IOP Publishing Measurement Science and Technology
Meas. Sci. Technol. **28** (2017) 015501 (14pp) doi:10.1088/1361-6501/28/1/015501

A novel TDR signal processing technique for measuring apparent dielectric spectrum

Chih-Ping Lin, Yin Jeh Ngui and Chun-Hung Lin

National Chiao Tung University, 1001 Ta-Hsueh Road, Hsinchu, Taiwan

E-mail: cplin@mail.nctu.edu.tw

Received 28 July 2016, revised 5 October 2016
Accepted for publication 27 October 2016
Published 1 December 2016

Abstract

Conventional time-domain reflectometry (TDR) signal interpretation generated single-valued apparent dielectric constant, while sophisticated, inconvenient measurement system and analysis is needed for measuring spectral complex dielectric permittivity (CDP). Niching between these approaches, a novel phase velocity analysis (PVA) method is developed to efficiently measure apparent dielectric spectrum (ADS) directly from TDR signals in a simple, quick, model-free, and inversion-free manner. The proposed PVA method extracts the two reflections from the top and end of the sensing probe by proper window selection and calculates their phase shift at each frequency, from which the phase velocity and corresponding apparent dielectric constant can be determined. Numerical and experimental results demonstrated that PVA is capable of measuring ADS in a frequency band, typically from 100 MHz–1 GHz. The effect of signal truncation was identified as the main cause of poor results outside the effective frequency band. Factors that affect the frequency band of effective ADS were numerically investigated. For highly dispersive materials, the end reflection pulse does not fully develop before the arrival of subsequent multiple reflections, resulting in severe truncation error and decreasing the upper frequency of effective ADS. Methods to estimate and extend the frequency band of effective ADS were further proposed. The simple procedures behind PVA, and its computationally efficient nature, make this method suitable for field monitoring. The resultant ADS is a potential improvement to current applications utilizing a travel time approach.

Keywords: phase velocity analysis, TDR, dielectric spectroscopy, apparent dielectric spectrum

(Some figures may appear in colour only in the online journal)

1. Introduction

Time-domain reflectometry (TDR) has shown dramatic developments over the past few decades. It has become a valuable tool in different fields, including material science [1, 2], soil physics [3, 4], structural [5, 6], hydrological [7], and geotechnical engineering [8–10]. These wide applications are mainly due to TDR's capability of measuring dielectric properties over a wide frequency range from sub-MHz to several GHz.

Dielectric permittivity is a frequency-dependent complex number used to describe both the amplitude and phase information when a material is exposed to a dynamic electromagnetic (EM) field, which is otherwise known as polarization. On condition that the energy does not restore in the polarization, the material reveals a relaxation spectrum [11]. Dielectric relaxation information is important for the study of chemical bonding and the intermolecular interactions of mixtures [12]. In material science research, broadband dielectric spectroscopy, including the TDR technique, has generated wide interest and has gone through several decades of development [13–19]. For more practical use, the apparent dielectric constant (K_a) of soils extracted by travel time analysis has received more attention in soil physics and geotechnical engineering in water content measurements [3, 9, 20–22].

Compared to complex dielectric permittivity (CDP), apparent dielectric constant is a practical definition based on travel time analysis (i.e. apparent propagation velocity of electromagnetic wave in the measured material). The

uncertainties in determining the apparent propagation velocity increase the measurement error in water content [23]. Chung and Lin [24] further examined the influence of electrical conductivity (EC), cable length, and dielectric dispersion on the apparent dielectric constant and the corresponding effective frequency. They concluded that the effective frequency varies with the influencing factors, and that it is difficult to compensate for these effects.

To go beyond the apparent dielectric constant approach, full waveform analysis considering dielectric relaxation was proposed. A better understanding of the TDR measurement system and dielectric properties of soils improved the modelling of the TDR waveform, making it possible for it to serve as the forward model for model-based inversion [8, 25–31]. In earlier works, Yanuka *et al* [31] incorporated multiple reflections, but neglected dielectric dispersion. Heimovaara [30] and Friel and Or [29] focused on dielectric dispersion (including conductive loss) by adapting a measuring system, which satisfied the condition of a uniform transmission line. However, practical measuring systems are much more complicated, especially in field conditions. A non-uniform transmission line model should be considered instead. Feng *et al* [28] and Lin [26] proposed non-uniform transmission line models including both multiple reflections and dielectric dispersion, but not the effect of conductor resistance. More recently, a comprehensive modelling of the TDR waveform was presented [32]. These forward models were developed based on the scatter function S_{11} [28] and input impedance [26], in which a recursive equation computed in a bottom-up fashion was derived to determine the final TDR response. However, recursive computations made it difficult to separate the leading sections from the sensing waveguide and resulted in a tedious and complex calibration procedure [33]. These techniques are not convenient enough to be applied in practice in the field.

There is a growing demand for developing an easy and efficient technology to measure dielectric spectrum [34–36]. Innovative methods, such as triple-short probe calibration [36], short-open-load calibration [35], and two different probe length approaches [34], were proposed to avoid the tedious calibrations of all transmission line sections in the system. Nonetheless, non-conventional exquisite probes were required and the calibrations for their applications were quite involved. The measurement of dielectric spectrum is still not an easy task to routinely perform.

The advantage of considering the frequency dependency was demonstrated by Lin [26]. Instead of time-domain K_a, the real part of CDP at a certain (optimal) frequency range has a much better correlation to water content independent of soil types. However, as addressed earlier, it is not practical to measure CDP in the field. Following the nomenclature used in Lin [26], a frequency-dependent 'apparent dielectric permittivity' is defined as the square of the ratio of the speed of light to the phase velocity of EM waves in the measured material. The propagation velocity of EM waves is frequency-dependent and is a function of the CDP. In fact, at frequencies over 100 MHz, the effect of EC is normally negligible, and apparent dielectric permittivity has the same value as the real part of dielectric permittivity when the frequency is away from the relaxation frequency. Between the time-domain K_a and full CDP approach, this study aimed to propose a phase velocity analysis (PVA) method that can effectively measure apparent dielectric permittivity in the frequency range from 100 MHz–1 GHz. This method starts by extracting two signals reflected from the beginning and the end of the TDR probe using appropriate window selection on the TDR waveform. Phase differences between the two signals at each frequency are then gathered to calculate the frequency-dependent propagation velocity of EM waves. No dielectric permittivity model is involved in the analysis and no calibration for system parameters is required. Due to these convenient characteristics, the proposed method is especially suitable for field applications.

The theory of PVA in apparent dielectric spectrum (ADS) determination is first elaborated. Next, both the numerical simulation and experimental verification of the PVA method are presented for five selected materials (distilled water, tap water, methanol, ethanol, and acetone). The truncation effect of the two signals, influenced by EC and dielectric dispersion, are revealed and discussed. Empirical countermeasures are proposed to define the reliable frequency range and further extend the workable frequency.

2. Phase velocity analysis

2.1. Propagation velocity of a transverse electromagnetic (TEM) wave

The equivalent dielectric permittivity ε^* of a partially conducting material can be written as [37],

$$\varepsilon^*(f) = \varepsilon'(f) + j\varepsilon^{ii}(f) = \varepsilon'(f) - j\left(\varepsilon''(f) + \frac{\sigma}{2\pi f\varepsilon_0}\right) \tag{1}$$

where f is the frequency; j is $(-1)^{1/2}$; ε' and ε'' are the real and imaginary parts of dielectric permittivity, respectively; ε^{ii} is the imaginary part of the equivalent dielectric permittivity, σ is the electrical conductivity, and ε_0 is the dielectric permittivity of free space. For non-ferromagnetic material, the propagation velocity V_{TEM} of an EM wave, which travels in a material with equivalent dielectric permittivity ε^*, can be written as [37],

$$V_{TEM} = \frac{c}{\sqrt{\frac{\varepsilon'}{2}\left[\sqrt{1+\left(\frac{\varepsilon^{ii}}{\varepsilon'}\right)^2}+1\right]}} \tag{2}$$

in which c is the speed of light. The propagation velocity is determined by the equivalent dielectric permittivity ε^*. Since ε^* is the function of frequency, the propagation velocity is hence frequency dependent. Compared to CDP, the denominator in equation (2) can be treated as the square-root of the apparent dielectric permittivity (ε_a) at each frequency.

2.2. Propagation, reflection and transmission of TEM waves

A typical TDR system consists of a pulse generator, oscilloscope, cabling, and a sensing probe. The pulse generator sends a step pulse into lead cables with a sensing probe as the last

section of the transmission line. The EM wave is transmitted into the measured material along the probe-sensing section. All the incidents and reflections, which occurred in the TDR system, were recorded by the oscilloscope. It is proven that the dominant mode of the TDR system is 1D TEM. Transmission line theory is hence used to model the system [28]. When the wave is propagating through the transmission line, decay and phase changes of the wave occur. This phenomenon is described by a propagation function H:

$$H(x, \varepsilon^*(f)) = \exp[-\alpha(f)x - jk(f)x] \tag{3}$$

where α is the attenuation constant and defined as

$$\alpha = \frac{2\pi f}{c}\sqrt{\frac{\varepsilon'}{2}\left[\sqrt{1+\left(\frac{\varepsilon^{ii}}{\varepsilon'}\right)^2}-1\right]} \tag{4}$$

whereas k is the phase constant (wavenumber) and defined as

$$k = \frac{2\pi f}{c}\sqrt{\frac{\varepsilon'}{2}\left[\sqrt{1+\left(\frac{\varepsilon^{ii}}{\varepsilon'}\right)^2}+1\right]} = \frac{2\pi f}{V_{\mathrm{TEM}}} \tag{5}$$

and x is the travelling distance.

Attenuation and phase changes of waves are not the only occurrences during wave propagations. Reflections and transmissions take place at discontinuities of characteristic impedance (Z_c). Characteristic impedance is a function of the cross-section geometry of the transmission line and the dielectric permittivity of the material. Z_c can be written as,

$$Z_c = Z_p/\sqrt{\varepsilon^*} \tag{6}$$

in which Z_p is the characteristic impedance of the transmission line section filled with air. For a probe with regular geometric cross-section, Z_p can be calculated from EM theory, but a calibration using material of known dielectric permittivity can also measure Z_p easily even for an arbitrary geometric cross-section. The reflection coefficient ρ_i and transmission coefficient τ_i at the interface between section i and section $i+1$ are defined as,

$$\rho_i = \frac{Z_{c,i+1} - Z_{c,i}}{Z_{c,i+1} + Z_{c,i}} \tag{7}$$

$$\tau_i = 1 + \rho_i \tag{8}$$

2.3. Relating reflections to propagation velocity of measured material

In a typical TDR system, two major discontinuities of characteristic impedance exist at the interface between the cable and probe, and the probe end. As shown in figure 1, an input X travelled along the cable, where F is the system function for forward propagation and B for backward propagation, which is then reflected from Interface I. The reflection pulse 1 (hereinafter referred to as R_1) is

$$R_1 = X \cdot F \cdot \rho_1 \cdot B \tag{9}$$

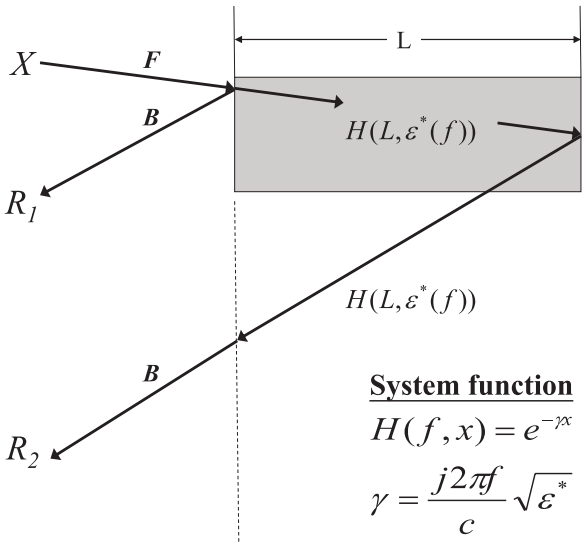

Figure 1. Ray tracing diagram for the first two TDR reflections.

Despite the reflection, a part of the forward wave is transmitted into the sensing probe and propagated to the probe end. During the transmission from Interface I to the probe end, the propagating wave is influenced by the material surrounding the probe. Changes at different locations along the path can be described by equation (3). Considering an open-ended probe, the reflection coefficient ρ_2 is equal to 1, according to equation (7). After travelling back from the probe end, the EM wave passes through the probe again. Upon reaching Interface I, the propagating wave transmitted to the cable and then travelled back along the cable. The reflection from the probe end is denoted as R_2. According to the propagating path described above, R_2 can be written as,

$$R_2 = X \cdot F \cdot (1+\rho_1) \cdot H(2L, \varepsilon^*(f)) \cdot (1-\rho_1) \cdot B \tag{10}$$

where L is the probe length. In equations (9) and (10), X, F, and B are the system parameters and not the targets being measured.

The dielectric information ε^* of interest is in $H(x, \varepsilon^*(f))$ and ρ_1. There is a simple way to deal with this. If we look at the phase term of R_2/R_1, the system parameters can be cancelled out for non-trivial scenarios. This can be expressed as,

$$\angle(R_2/R_1) = \varphi_\rho - 2kL \tag{11}$$

in which $\angle$ is the operator of the taking angle; the term $2kL$ is the phase shift due to $H(2L, \varepsilon^*(f))$; φ_ρ is the phase perturbation caused by the reflection coefficient and is defined as,

$$\varphi_\rho = \angle\left(\frac{1-\rho_1^2}{\rho_1}\right) \tag{12}$$

From equation (5), the propagation velocity of the material filled within the probe can be reformulated as,

$$V_{\mathrm{TEM}} = \frac{4\pi fL}{\varphi_\rho - \angle(R_2/R_1)} \tag{13}$$

Here, φ_ρ is undermined without knowing the CDP of the material under test. It is typical to design the sensing probe to

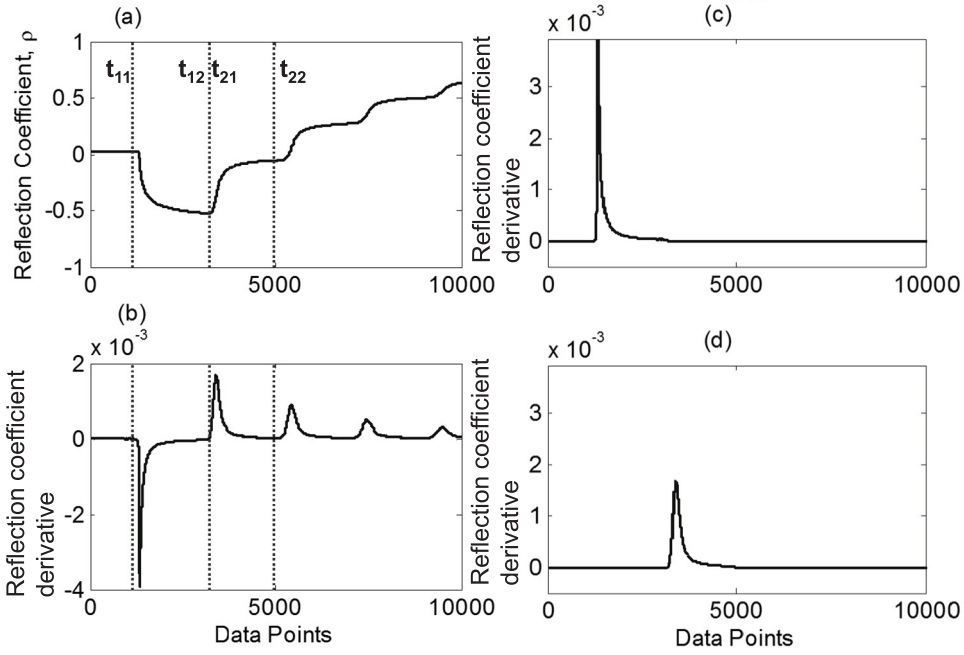

Figure 2. (a) Typical TDR signal in water; (b) differentiated waveform of (a); (c) and (d) extracted reflection pulse 1 ($-R_1$) and pulse 2 (R_2), respectively.

have characteristic impedance lower than that of the leading cable, ρ_1 and hence $(1-\rho_1^2)/\rho_1$ are negative. Considering only the real part of CDP, φ_ρ is equal to π. The imaginary part of CDP would make φ_ρ slightly different from π. However, compared to $\angle(R_2/R_1)$, this difference is negligible, especially at higher frequencies. Hence, the propagation velocity can be approximated by the following velocity definition:

$$V_{\mathrm{PVA}} = \frac{4\pi fL}{\pi - \angle(R_2/R_1)} = \frac{4\pi fL}{\angle(-R_1/R_2)} \cong V_{\mathrm{TEM}}. \qquad (14)$$

The term $\angle(-R_1/R_2)$ represents the phase shift between the two reflections and is also denoted and referred to as $\Delta\phi$. The velocity from the above PVA (V_{PVA}) can be computed directly from reflection pulses (R_1 and R_2) extracted from the TDR waveform. This is the theoretical basis for the proposed PVA method.

2.4. Signal processing

As shown in equation (14), R_1, R_2, and L are the three inputs for the proposed method. L can be measured directly from the probe. However, R_1 and R_2 have to be extracted from the TDR waveform. A signal processing is proposed here to implement the idea. A typical TDR waveform measured in water (as shown in figure 2(a)) is used to illustrate the procedure.

(1) Differentiation of TDR step pulse signal into impulse signal (as shown in figure 2(b)).
(2) Reflection pulse extraction: the most important procedure for this proposed method is to extract R_1 and R_2. R_1 and R_2 are the reflections from the interface between the cable and probe, and the probe to the probe end. They can be easily identified from the waveform. However, the conundrum is to determine the best time window span for each pulse. A pulse-extraction strategy called Normal-Time-Window is suggested here. The start of the time-window span for R_1 is suggested to be close to the probe head denoted as t_{11} in figure 2(b). There is no difference for where the t_{11} is located if the TDR signal before the sensing probe is flat. The end of R_1 (t_{12}) is suggested to be the lowest reflection coefficient in figure 2(a). At this time location, the derivative signal would generally pass through zero value. The start of the time span for R_2 (t_{21}) is set to be equal to the end of R_1. The end of R_2 (t_{22}) is suggested as the zero point before the next multiple reflection, as shown in figure 2(b). Sometimes, the differentiated signal may not reach the zero point before the next reflection. In such cases, the lowest point between R_2 and R_3 is suggested as t_{22} instead.
(3) Reversing R_1 and zero-padding on both reflections: Revisiting equation (14), there is a π term in the denominator. For convenience, we dealt with this term by reversing R_1 vertically, as shown in figure 2(c). In order to maintain good frequency resolution, zero-padding on both reflections is recommended, as shown in figures 2(c) and (d).
(4) Performing fast Fourier transform on two extracted pulses R_1 and R_2, and computing the phase angle.
(5) Calculating the phase shift $\Delta\phi = \angle(-R_1/R_2)$.
(6) Calculating phase velocity V_{PVA} by equation (14).
(7) Calculating apparent dielectric permittivity $\sqrt{\varepsilon_{\mathrm{a}}(f)}$ from the phase velocity,

Table 1. Cole–Cole parameters of MUTs selected for TDR waveform simulation.

MUT	Abbreviation	ε_{dc}	ε_{∞}	f_{rel} (GHz)	σ_{dc} (μS cm^{-1})	β
Distilled water [29]	DIS	80.20	4.22	17.4	0	0.0125
Tap water [29]	TAP	78.54	4.22	17	300	0.0125
Methanol [40]	MTH	33.64	5.70	3.002	0	0
Ethanol [41]	ETH	25.50	4.25	0.782	0	0
Acetone [40]	ACE	21.20	1.90	47.65	0	0

$$\sqrt{\varepsilon_a(f)} = \frac{c}{V_{PVA}(f)} = \sqrt{\frac{\varepsilon'}{2}\left[\sqrt{1+\left(\frac{\varepsilon^{ii}}{\varepsilon'}\right)^2}+1\right]} \quad (15)$$

It can be seen that no system calibration and no inversion are involved during measurement of the apparent dielectric permittivity. This enables the proposed PVA to be highly convenient and computationally efficient. The proposed method can be easily applied in field measurements and provide real-time ADS from measured TDR time domain signals.

3. Numerical evaluation and investigation of PVA

3.1. Performance evaluation in synthetic data

Synthetic TDR waveforms of five selected materials under test (MUT) were simulated, namely distilled water, tap water, methanol, ethanol, and acetone. These MUTs were selected to evaluate the performance of and to validate the proposed PVA method in materials with different dielectric dispersion characteristics and electrical conductivity. For comparison between numerical simulation and experimental data, the system parameters of simulation were selected to be similar to the experimental setup. A three-section transmission line model was simulated, consisting of a 42 m 50 Ω coaxial cable, a 0.1 m 50 Ω matched probe head, and a 0.17 m coaxial probe-sensing section.

Numerical simulation was performed according to the formulations presented in the previous section and a comprehensive wave propagation model established by Lin and Tang [32], which recursively derives characteristic impedance of each section from terminal impedance to source impedance. Both the propagation function, H, and characteristic impedance, Z_c, of the transmission line components are dependent on the frequency-dependent CDP, $\varepsilon^*(f)$, which is characterized by the Cole–Cole function [38]

$$\varepsilon^*(f) = \varepsilon_{\infty} + \frac{\varepsilon_{dc}-\varepsilon_{\infty}}{1+\left(jf/f_{rel}\right)^{1-\beta}} - \left(\frac{j\sigma}{2\pi f\varepsilon_0}\right) \quad (16)$$

where ε_{∞} and ε_{dc} are dielectric constants at the frequency of infinite and static condition respectively, ε_0 is the dielectric permittivity of free space; f_{rel} is the relaxation frequency, and β is the symmetrical shape parameter of dielectric loss spectrum. MUTs were also defined by this dielectric model, assuming symmetric broadening of their dielectric loss peak. Cole–Cole function parameters of the MUTs are listed in table 1, with their corresponding abbreviation used hereinafter.

Characteristic impedances, Z_c, of both the coaxial cable and matched probe head were simulated as 50 Ω by assuming both Z_p as 50 Ω and their dielectric permittivity $\varepsilon^*(f)$ as 1 throughout the dielectric spectrum. Z_p of the coaxial probe-sensing section was computed as 95 Ω by assuming that the coaxial probe was in air ($\varepsilon^* = 1$), using the following characteristic impedance determination equation [39]

$$Z_c = \frac{1}{2\pi}\sqrt{\frac{\mu_0}{\varepsilon_0\cdot\varepsilon^*}}\ln\frac{D}{d} \quad (17)$$

where μ is the magnetic permeability, μ_0 is the vacuum permeability, D is the inner diameter of the external conductor, and d is the outer diameter of the internal conductor.

Full TDR waveforms were simulated with 5 ps sampling time and the total simulation time window was $8.8323 * 10^{-7}$ s. Simulated time-domain signals of the five materials shown in figure 3 were truncated from 1 m before the probe-sensing section for presentation clarity. The simulated signals were processed according to the elaborated PVA signal-processing procedure, adopting the Normal-Time-Window pulse extraction strategy. Five analyzed waveforms were zero-padded to 2^{14} data points to increase the frequency resolution under the constant sampling interval. The resultant ADS, ε_a, is illustrated in figure 4, with a targeted 10 MHz–1 GHz frequency range, as this spectral region is the typical effective frequency of TDR signals.

PVA-generated ADS for the MUTs match their corresponding theoretical values (marked as lines) well within a certain frequency range. It was noted that the reliable frequency ranges of PVA measured data were different for each MUT, which were caused by the signal truncation effect. The truncation effect is induced by two influencing factors including EC and dielectric dispersion. In order to estimate the reliable spectral boundaries of the PVA measured data, the aforementioned factors inducing signal truncation are further discussed in the following sections.

3.2. ϕ_ρ error and truncation effect from EC

EC, σ causes some phase shift to φ_ρ, which otherwise is equal to π, in equation (13) and conductive loss due to EC is significant at lower frequencies. The PVA method may incorrectly predict ε_a at lower frequencies and hence the obvious plunge at the lower frequency of the tap water (300 μS cm^{-1}) in figure 4. To illustrate the degree of conductive loss due to EC, the imaginary part of the dispersion curve modelled from theoretical Cole–Cole CDP was taken and plotted in

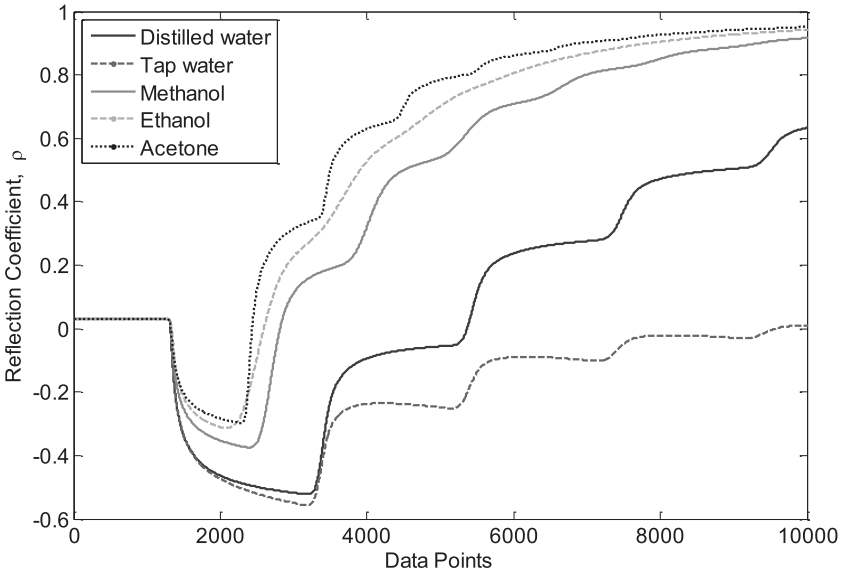

Figure 3. Simulated TDR waveforms for MUTs in table 1.

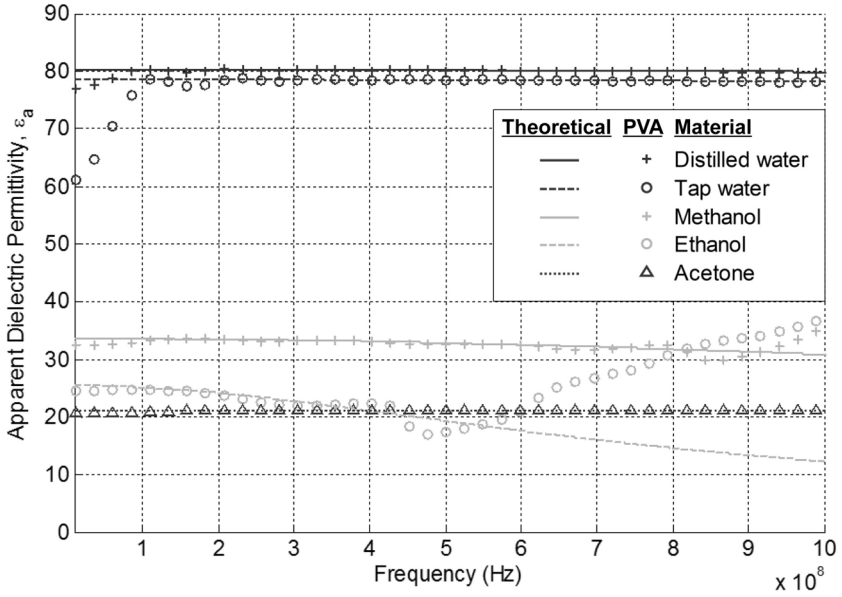

Figure 4. Comparison of PVA computed values and theoretical values.

figure 5(b). The EC-induced loss is significant at frequencies less than 100 MHz for this simulated case of the 0.17 m coaxial probe. However, the typical lowest frequency limit is dependent on the window length of the two truncated pulses. Detailed delineation of the lowest reliable limit of the PVA is discussed later.

The effect of EC on the TDR signals reflects on the steady state of step reflection. Higher EC delays the time needed for the reflected pulses to reach the steady state, causing leakage of R_1 into R_2, as shown in figures 5(c) and (d). Signal truncation on these types of signals had higher impact due to the occurrence of end truncation of reflection pulse 1 (R_1). To demonstrate the signal truncation effect from EC, we simulated ideal R_1 and R_2 of a 300 μS cm^{-1} tap water based on equations (9) and (10) to denote the ideal reflections from the top and bottom of the coaxial probe received at the source oscilloscope, illustrated as dotted-lined waveforms in figures 5(c) and (d). This ideal case simulated the scenario where R_1 does not affect R_2 by pulse leakage of lower frequencies (longer travel time). Comparing the Normal-Time-Window extracted R_1 and R_2 from the TDR signal (denoted as solid-lined waveforms) to the ideal ones, TDR R_1 signal did not reach the steady state before the reflected TDR R_2 signal was received at the oscilloscope, and there was an obvious drop between TDR R_2 and ideal R_2 due to leakage of TDR R_1 (negative reflection) into TDR R_2.

By performing standard PVA on both the ideal and truncated TDR signals, the result was shown in figure 5(a) for tap water of 0 and 300 μS cm^{-1}, correspondingly denoted by '+' and 'o' symbols. PVA-generated ADS generally matches the actual ADS modelled by the Cole–Cole function, but it is only correct beyond certain frequencies inversely proportional to the time between the arrival onsets of R_1 and R_2,

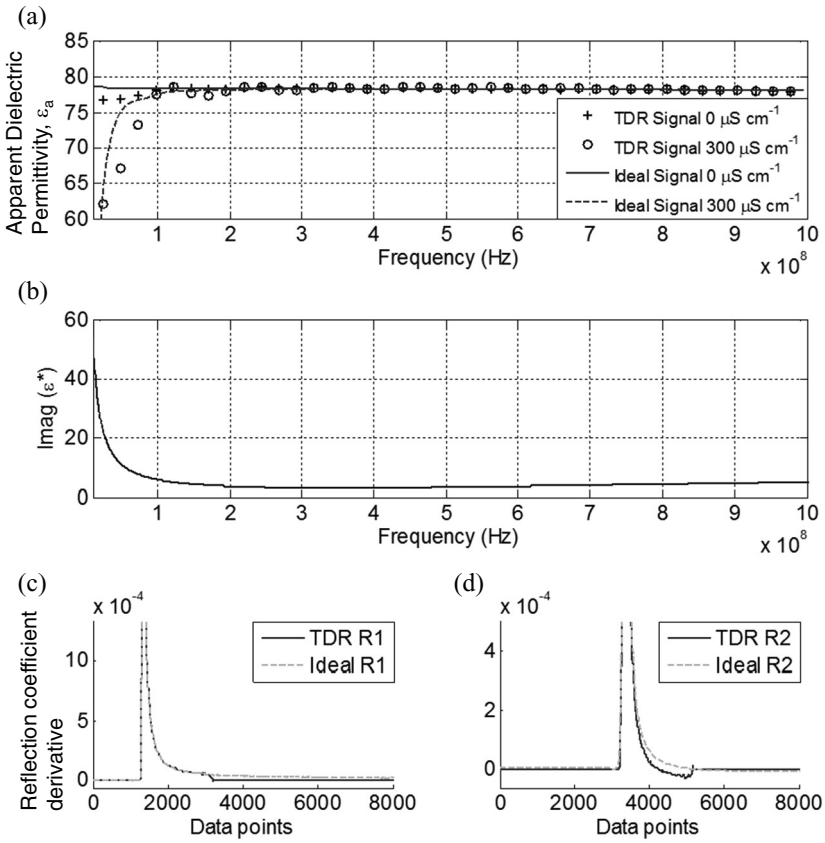

Figure 5. Influence of EC in water: (a) error induced in ADS, (b) imaginary part of frequency-dependent dielectric permittivity, $\varepsilon^*(f)$ of 300 μS cm^{-1} tap water, (c) and (d) comparison of ideal reflection pulses and extracted TDR waveforms for R_1 and R_2, respectively, in 300 μS cm^{-1} tap water.

which is physically related to the sensing-probe length. The ideal signals, therefore, actually diverged at the same point from the truncated TDR signals, but the plunging amounts of the two ideal signals are less significant than the TDR signals due to the absence of pulse leakage. The higher the material's EC, the higher the conductive loss induced and the plunging amount of ADS at lower frequencies. ADS of truncated TDR signals at higher frequencies oscillated within ± 0.5, which is introduced by an undesirable high-frequency component during pulse truncation.

3.3. Truncation effect from dielectric dispersion

Apart from the truncation effect due to EC, dielectric dispersion of MUT induces dielectric loss and amplifies the truncation effect in TDR signals, particularly in R_2. This phenomenon is substantial in the case of the high dielectric permittivity drop within the targeted TDR frequency range (100 MHz–1 GHz) and when the relaxation frequency of the material lies near the targeted frequency range. Both dielectric drop ($\Delta\varepsilon_a$) and relaxation frequency (f_{rel}) could be in multiple combinations (small $\Delta\varepsilon_a$ and low f_{rel}, large $\Delta\varepsilon_a$ and high f_{rel}, and so on) to cause a similar amount of dielectric dispersion within the targeted frequency range. The TDR signal is generally highly influenced by material dielectric dispersion within 100 MHz–1 GHz. For simplification and clarity when dealing with the dielectric dispersion effect on PVA, we focused on the amount of dielectric constant drop within the major TDR frequency range ($\Delta\varepsilon_{TDR}$), defined as

$$\Delta\varepsilon_{TDR} = \varepsilon_{1\,GHz} - \varepsilon_{0.1\,GHz} \tag{18}$$

where $\varepsilon_{0.1\,GHz}$ and $\varepsilon_{1\,GHz}$ are the dielectric constant measured or modelled at 100 MHz and 1 GHz, respectively. $\Delta\varepsilon_{TDR}$ is a useful index in quantifying the degree of dielectric loss in TDR signals due to dielectric dispersion. To demonstrate the truncation effect from dielectric dispersion, two cases of different dispersion degrees with insignificant EC are discussed. Methanol with mild dielectric dispersion has a $\Delta\varepsilon_{TDR}$ of 2, and ethanol with high dielectric dispersion has a $\Delta\varepsilon_{TDR}$ of 11, in which both materials have insignificant EC value. Tap water has low dielectric dispersion within the TDR PVA range, of which $\Delta\varepsilon_{TDR}$ is only 0.3 and hence the sharp interface reflections at the probe end.

For methanol with mild dielectric dispersion of $\Delta\varepsilon_{TDR} = 2$ and EC $= 0$ μS cm^{-1}, the maximum dielectric loss occurred near 1 GHz, as can be seen in figure 6(b), where the plotted imaginary part of CDP $\varepsilon^*(f)$ reached the maximum loss. Compared to ethanol, methanol produced fewer dispersive signals and its multiple reflections were relatively stronger, as can be seen in figure 3. Similar to the EC truncation effect discussion, the ideal R_1 and R_2 signals (denoted as dotted lines) of methanol were simulated to further visualize the truncation effect of dielectric dispersion in figures 6(c) and (d). The signal truncation of R_1 was less problematic due to the absence of EC, and so the steady state was reached faster than with tap water.

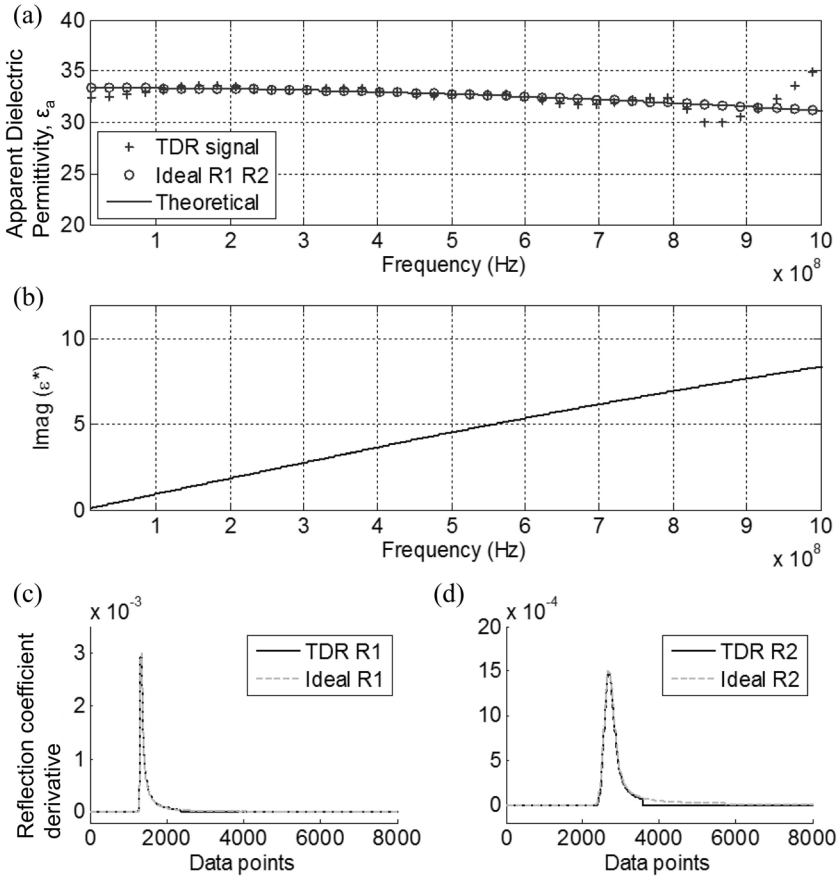

Figure 6. Influence of mild dielectric dispersion to TDR signal truncation in methanol: (a) truncation error in ADS, (b) imaginary part of frequency-dependent dielectric permittivity, $\varepsilon^*(f)$, (c) and (d) comparison of ideal reflection pulses and extracted TDR waveforms for R_1 and R_2, respectively.

The R_2 end truncation is the main issue in the signal truncation of dispersive materials as the TDR signal reflections would be flatter, induced by dielectric loss. This can be observed from the common trend of ADS, where the dielectric constant is significantly lower in high frequency than low frequency for dispersive materials, causing various frequency components to travel at different phase velocities and disperse into flatter, distorted waveforms. Figure 6(a) shows the ADS of both the ideal signal and truncated TDR signal from PVA compared to the theoretical values of methanol. Since PVA on ideal signals matched the theoretical values accurately throughout the TDR spectrum, the ADS oscillation near 800 MHz, which occurred in the truncated signal, was indeed the outcome from the slight drop of truncated R_2, as shown in figure 6(d). Even though the relaxation frequency for methanol is at 3.002 GHz, the $\Delta\varepsilon_{\mathrm{TDR}}$ of methanol is 2 and the dielectric dispersion due to dielectric drop became prominent, leading to the possible signal truncation of R_2. Nevertheless, the workable bandwidth of PVA was still wide for at least 800 MHz in methanol.

Ethanol has a high dielectric loss of $\Delta\varepsilon_{\mathrm{TDR}} = 11$ mainly because its relaxation frequency lies at 782 MHz, causing the maximum dielectric loss to occur within the TDR range. Figure 7(b) is the imaginary part of CDP $\varepsilon^*(f)$ modelled by the Cole–Cole function of ethanol, illustrating that the maximum point of dielectric loss spectrum matched the onset of ADS oscillation for the TDR signal of ethanol in figure 7(a). Ideal R_1 and R_2 signals for ethanol were again simulated to inspect the severity of the truncation effect due to dielectric loss. TDR signals of the highly dispersive ethanol are even flatter compared to methanol, as a dispersive ADS, as previously mentioned, would lead to further separation of the frequency components. By applying Normal-Time-Window to truncate the ethanol TDR signals for PVA, the R_2 end truncation of ethanol is significant when comparing TDR R_2 to ideal R_2 in figure 7(d), which introduced a sudden drop in the extracted R_2 pulse. Figure 7(a) compared the ADS of the ideal signal, truncated TDR signal, and theoretical value for ethanol. PVA-generated ADS for the ideal signals fitted the theoretical values well even for the spectral range near the relaxation frequency of 780 MHz. However, due to the end truncation of the TDR R_2 waveform and introduced unwanted frequency components, a sudden jump occurred in the TDR signal's ADS and shortened the correct PVA frequency range down to 300 MHz by manual inspection. To extend the reliable frequency range, a countermeasure in the form of the Long-Time-Window method is proposed, after delineating the reliable bound of PVA-generated ADS.

3.4. Reliable bound of PVA-generated ADS

The truncation effect from TDR signal extraction is inevitable, and reliable bound delineation of PVA-generated ADS

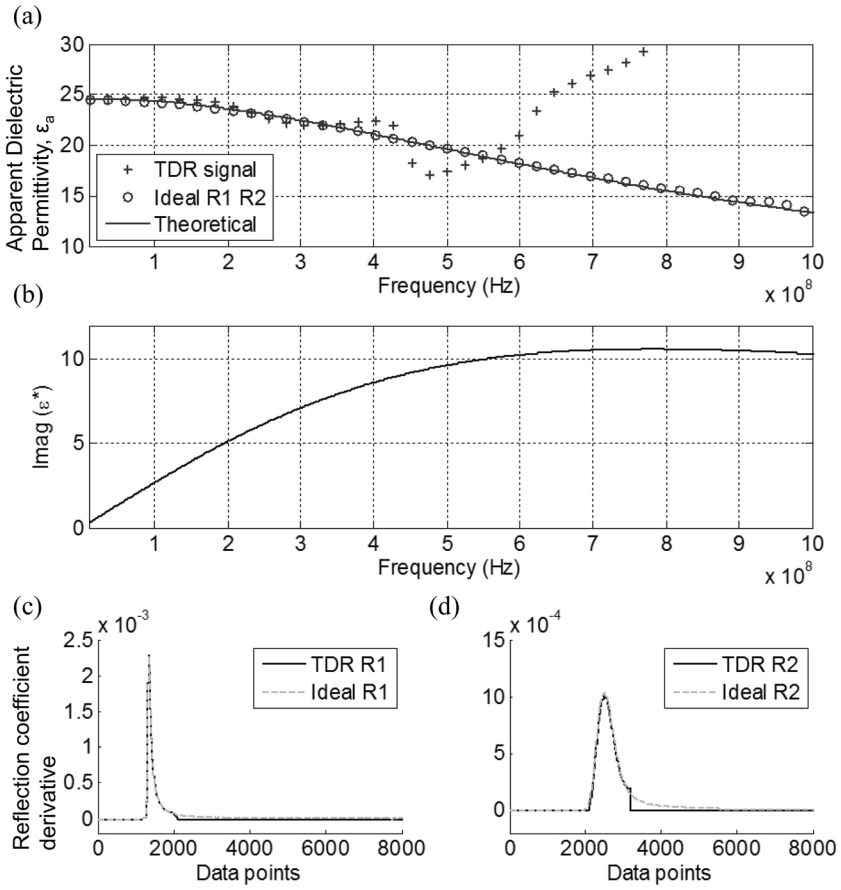

Figure 7. Influence of high dielectric dispersion to TDR signal truncation in ethanol: (a) truncation error in ADS, (b) imaginary part of frequency-dependent dielectric permittivity, $\varepsilon^*(f)$, (c) and (d) comparison of ideal reflection pulses and extracted TDR waveforms for R_1 and R_2, respectively.

is discussed here for appraisal of the result. A lower frequency limit of effective ADS is mainly controlled by workable wavelength ($\lambda_{\text{workable}}$) due to signal truncation. The lower frequency limit is dependent on the length of the two truncated pulses, which is physically related to the probe length. Since recorded TDR signal is a combination of forward and backward propagating wave, the maximum wavelength is twice the probe length. The lower frequency limit of effective ADS, f_{lower}, can be computed from the physical probe length by

$$\lambda_{\text{workable}} = 2 \times L \tag{19}$$

$$f_{\text{lower}} = V_{\text{PVA}}(f)/\lambda_{\text{workable}} \tag{20}$$

where L is the sensing-probe length.

The upper frequency limit of effective ADS is relatively complicated as several influencing factors are involved: relaxation frequency, dielectric drop within 100 MHz and 1 GHz ($\Delta\varepsilon_{\text{TDR}}$), R_2 end truncation and signal noise. Analytical definition is impossible and a data-based algorithm in the phase angle domain was proposed to delineate the effective upper limit. Upon determining the lower limit from equation (20), a third-degree poly-fitting is applied to the frequency range between the computed lower limit to 1 GHz in $\Delta\phi - f$ domain. The frequency in which the difference between the experimental $\Delta\phi(f)$ curve and fitted $\Delta\phi(f)$ curve exceeds 0.5 is suggested to be the upper frequency limit of effective ADS. The upper limit determination for distilled water and ethanol in $\Delta\phi - f$ domain is shown in figure 8(b), with solid lines as the third-degree poly-fitting curve, and the left-pointing solid triangles as the computed upper limit. The proposed PVA reliable bound determination was performed on all simulated data, from which the outcomes of the lower and upper limits were plotted in figure 8(a) as right-pointing and left-pointing solid triangles, respectively. Nonetheless, the upper limit can be determined easily through straightforward visual inspection on the ADS for the frequency bound, where data oscillation becomes significant.

The reliable frequency range of simulated ethanol data in figure 8(a) was narrower than other MUTs due to high dielectric dispersion. Consequently, the Long-Time-Window countermeasure method is next proposed to extend the reliable frequency range for such cases.

3.5. Countermeasure of short reliable ADS: Long-Time-Window approach

PVA-generated relatively short reliable ADS in dispersive materials due to the end truncation of the second reflection. The Long-Time-Window approach is proposed to extend the reliable range in the dispersive materials by prolonging the time-window selection for the end of R_2 (t_{22}) to the full recording window. There is no change in the selection method

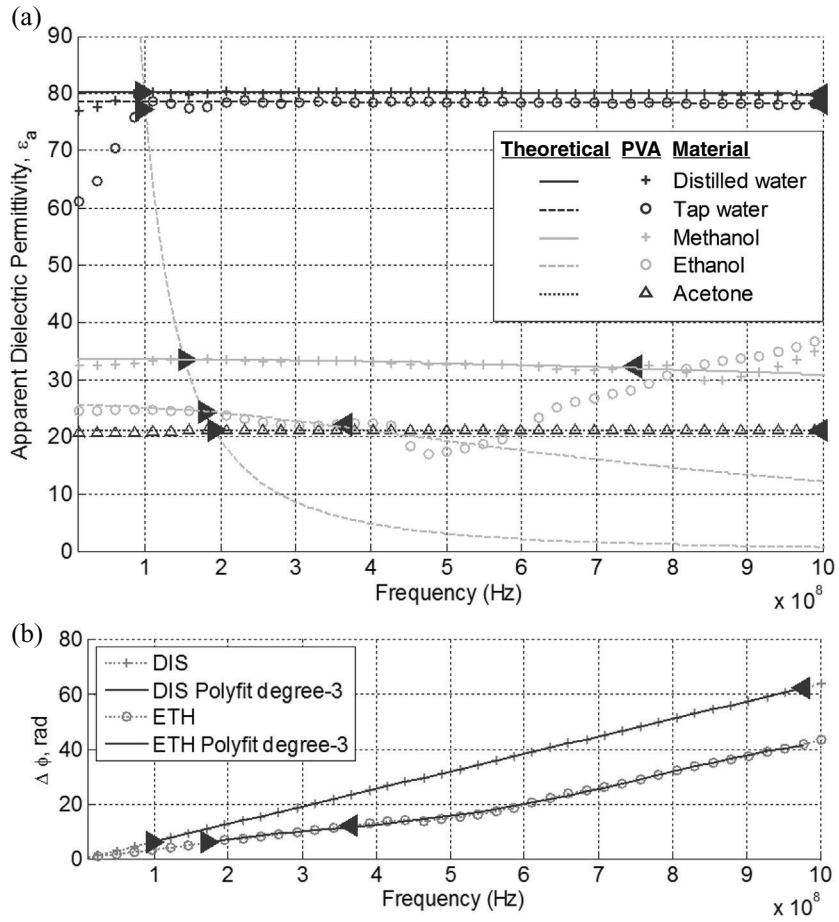

Figure 8. (a) Apparent dielectric permittivity with lower limit and upper limit marks. (b) Upper limit determination by third-degree poly-fitting in $\varphi_p - f$ domain.

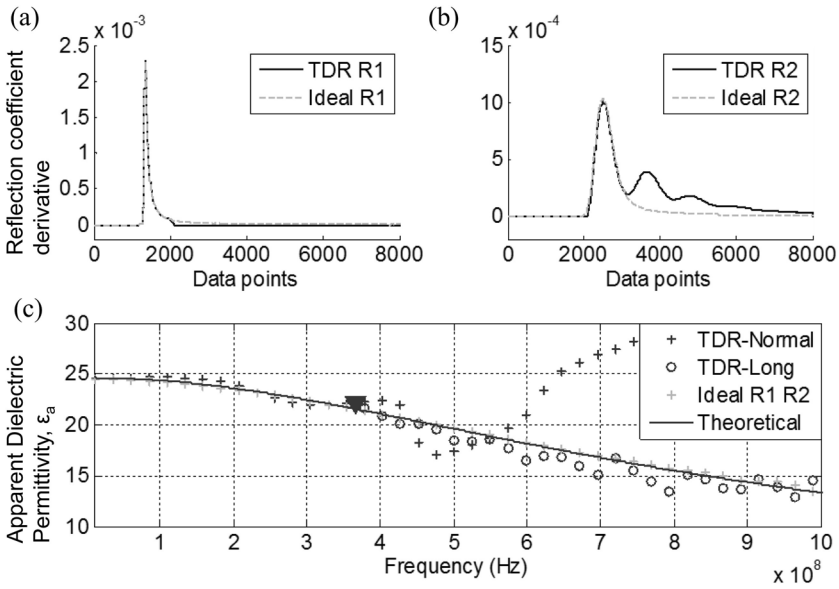

Figure 9. Long-Time-Window approach for highly dispersed signal in ethanol: (a) and (b) comparison of ideal reflection pulses and extracted TDR waveforms (by using Long-Time-Window) for R_1 and R_2 (c) reliable region for Normal-Time-Window (left of the ▼ mark) and Long-Time-Window (right of the ▼ mark) in apparent dielectric permittivity.

for R_1. The only difference is the time-window selection for R_2, as shown in figure 9(b), in which the end of R_2 is extended further towards the end which is closer to zero value. This method reduced the R_2 end truncation, while it concurrently included the multiple reflections after R_2. Since multiple reflections were incorporated into signal analysis, a side effect was reflected on the oscillation of the new ADS (denoted as 'o' symbol) along the theoretical values of higher frequencies

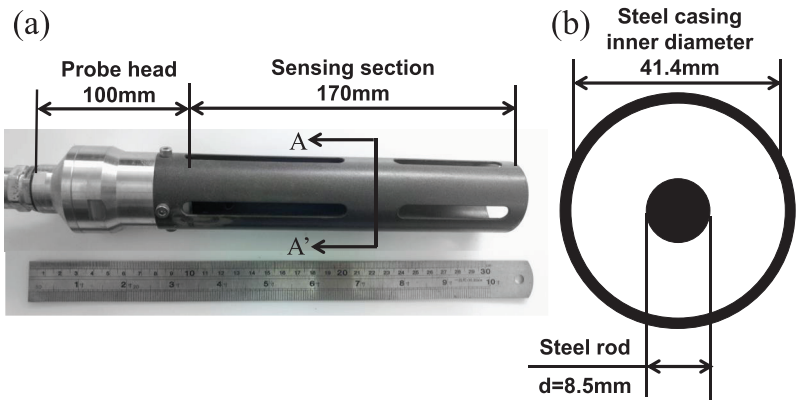

Figure 10. (a) TDR-matched coaxial probe, (b) cross-section of A–A′ in (a).

in figure 9(c). There is a compromise in ADS oscillation at higher frequencies due to multiple reflections, in an effort to extend the ADS short workable bandwidth due to the truncation effect. Long-Time-Window is not suitable for mild dispersive materials, because in such materials the multiple reflections are stronger and shaper, resulting in unacceptable errors in ADS.

The upper limit computed using Normal-Time-Window (denoted as a solid triangle in figure 9(c)) is established as the valid lower limit of Long-Time-Window. As shown in figure 9(c), left of the solid triangle is the reliable ADS generated using Normal-Time-Window, while right of the mark is the relatively accurate ADS generated by Long-Time-Window, denoted as 'o' symbol. By combining both pulse extraction methods, a wider reliable frequency range for ADS of highly dispersive materials could be achieved with minor trade-off of slight ADS oscillation.

4. Experimental verification of PVA

The PVA method was further verified by measuring experimental TDR waveforms of distilled water, tap water, methanol, ethanol, and acetone, using a self-developed TDR matched coaxial probe.

The experimental setup comprised a broadband TDR reflectometer with 3 GHz bandwidth, an N to BNC connector, a 50 Ω coaxial cable and a modularized stainless steel matched 50 Ω coaxial probe. Time-domain measurements were performed by generating a step EM pulse with a short rise time (10%–90%) of 80 ps, into the matched stainless steel probe via the 42 m coaxial cable and N to BNC connectors. TDR data on five MUTs were acquired using 5 ps sampling time under room temperature of 20 °C (±1 °C).

The matched coaxial sensing probe was manufactured from stainless steel into a 100 mm modularized 50 Ω matched probe head and a 170 mm coaxial sensing section comprising an internal conductor rod and a cylindrical external conductor casing. The matched coaxial probe configuration and cross-section geometry are shown in figure 10. The modularized probe head enabled the open-ended internal rod to be fixed at the centre and the probe components to be easily replaced if damaged. Equally spaced openings were perforated on the cylindrical casing to allow MUT to fill up the whole sensing section when immersed. The probe head is impedance-matched to the coaxial cable to avoid unwanted reflections in the PVA.

TDR waveforms of the five MUTs were acquired with the aforementioned setup to minimize the temperature effect on the ADS measurement. Figure 11 shows the time-domain waveforms measured using the open-ended matched coaxial probe, in which the illustrated waveforms were truncated from 1 m before the probe head. Ambient noise levels were suppressed with a 12 average waveform stacking for each signal. By initial inspection, the experimental waveforms matched closely to the simulated waveforms, but with some added noise.

Accurate ADS requires accurately determined probe length. The accuracy of the manually measured probe length may not be sufficient. Hence, the probe-length calibration by PVA is highly recommended for accurate results. Probe-length calibration is only required once by measuring a material with known dielectric spectrum. Tap water is normally adopted as it is a readily available material with well-established dielectric spectrum. In this study, the effective probe length was calibrated as 172.00 mm in tap water at 25 °C. The calibrated probe length was next adopted in PVA of other data sets at the same room temperature.

ADS of all MUTs computed from PVA with the Normal-Time-Window approach were plotted in figure 12(a). PVA measurements of each MUT were shown in various hollow symbols. Theoretical ADS modelled by the Cole–Cole function were also plotted as lines for verification. Lower and upper limits for each MUT were determined and marked as a right-pointing and left-pointing solid triangle, respectively, to illustrate reliable regions of the PVA.

Upon implementing the PVA procedures with Normal-Time-Window, all ADS matched the theoretical values closely within the delineated reliable region. Some slight oscillation of the ADS occurred due to ambient noise as no noise filtering or frequency manipulation was performed throughout the PVA. Apart from the lower and upper limits provided by the aforementioned approach, visual inspection in ADS for sudden jumps and obvious anomalies was quick and easy to delineate the PVA reliable frequency range of MUT.

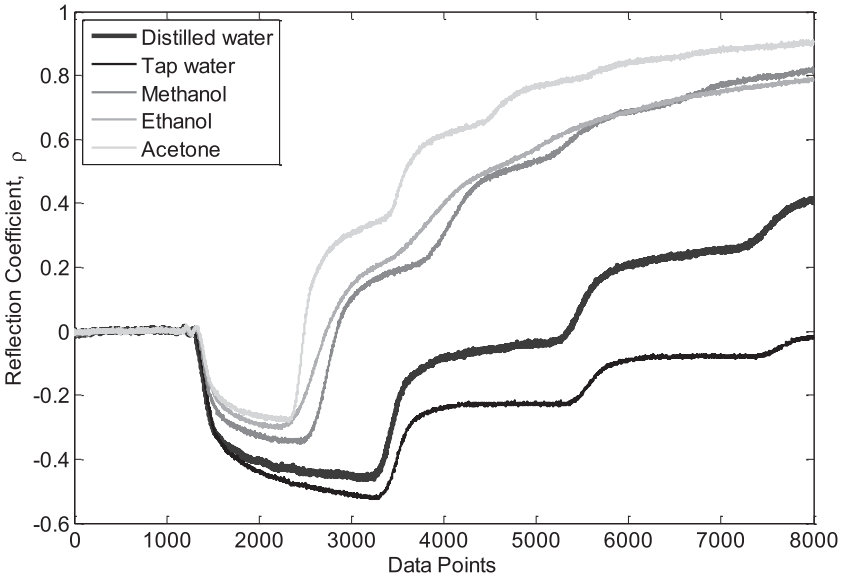

Figure 11. Experimental TDR signals.

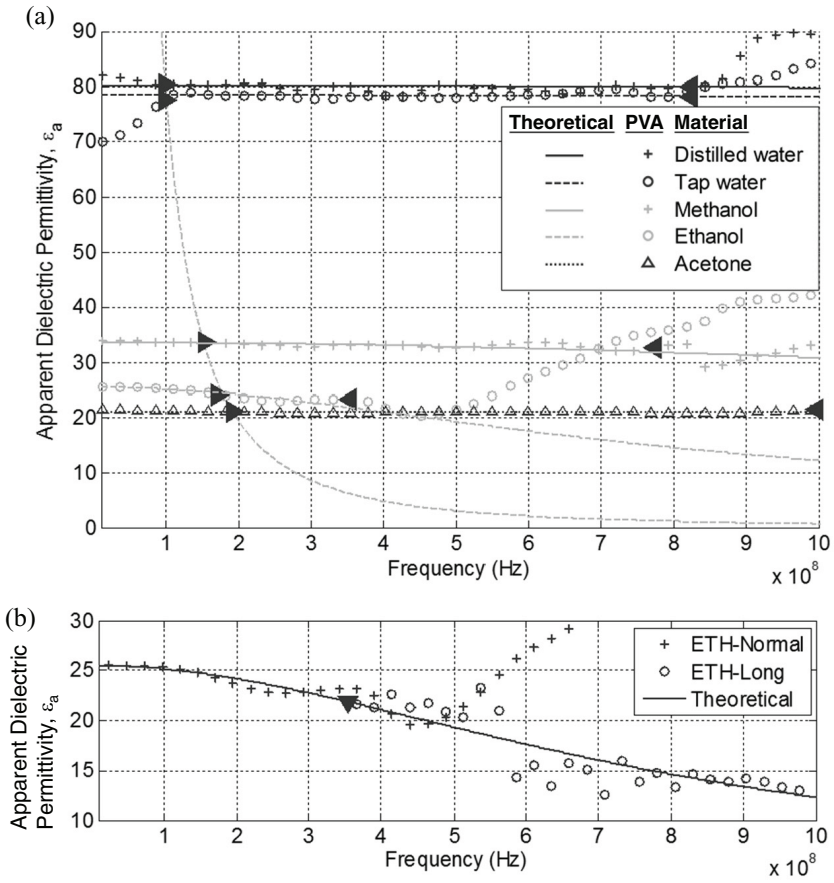

Figure 12. Experimental data: (a) comparison of PVA computed values (Normal-Time-Window) and theoretical values, (b) reliable region for Normal-Time-Window (left of the ▼ mark) and Long-Time-Window (right of the ▼ mark) in apparent dielectric permittivity of ethanol.

The upper limits of the distilled and tap water were slightly reduced compared to the simulated data, which may be caused by ambient noise and physical frequency filtering effect due to the precedent long coaxial cable, leading to the loss of high frequency information. As for methanol, ethanol, and acetone, their upper limits were similar to the simulated data, since their dielectric drop within the targeted region was the major controlling factor. Particularly for methanol and ethanol, with relaxation frequencies which lie near 1 GHz, their dielectric losses are relatively higher than the other three materials, leading to highly dispersive TDR signals and more significant R_2 end truncation during the PVA pulse extraction stage, hence inducing sudden ADS deviation beyond a certain frequency. These undesirable high-frequency results introduced

by pulse truncation can be further mitigated by performing the Long-Time-Window approach. In figure 12(b), an additional Long-Time-Window approach was conducted on ethanol to extend the reliable range of ADS from 200 MHz–1 GHz, since ethanol is a highly dispersive material within the 100 MHz–1 GHz range.

Good correlation of PVA experimental data with theoretical values demonstrated the reliability, simplicity, and efficiency of this proposed signal-processing method. This model-free, inversion-free, and pure signal-processing approach allowed researchers to economically measure accurate frequency-dependent ADS both in the field and laboratory, within a certain bounded reliable region.

5. Conclusions

This study proposed a novel method of PVA to determine ADS from TDR signals in a simple, quick, model-free, and inversion-free manner. PVA efficiently offers apparent dielectric permittivity with frequency content, which niches between time-domain approach (single-valued dielectric constant, fast) and vector network analyzer (spectral CDP, tedious).

The proposed PVA method extracts the two reflections from the top, and the end of the probe-sensing section by proper window selection and calculates their phase shift at each frequency, from which the phase velocity and corresponding apparent dielectric constant can be determined. TDR signals of the materials with different dielectric dispersion characteristics and EC were numerically simulated to validate this new approach and investigate factors which affect its performance. The results show that PVA-generated ADS matches the theoretical values well within a certain frequency range. The effect of signal truncation was identified as the main cause of poor results outside the effective frequency band. The effect of signal truncation depends on EC and the amount of dielectric dispersion within the TDR frequency band. The probe length and EC control the lower frequency limit of effective ADS, which could be below 10 MHz for non-conductive materials and about 100 MHz for typical EC. The reliability of ADS at higher frequencies is mainly controlled by the amount of dielectric dispersion within the TDR frequency range. The upper frequency limit of effective ADS is low for highly dispersive materials, because the end reflection pulse could not fully develop within the selected time window before the arrival of subsequent multiple reflections, resulting in severe truncation error. A countermeasure was proposed to extend the reliable frequency range in highly dispersive materials by prolonging the time window for the end reflection at the cost of minor ADS oscillation due to the inclusion of multiple reflections in the prolonged window.

The proposed PVA method was also validated by experiments. Experimental results agree well with numerical results, demonstrating PVA's capability of measuring ADS from 100 MHz–1 GHz. PVA efficiently measures spectral apparent dielectric constant directly from TDR signals without complicated modelling and system calibration, making it especially suitable for field monitoring. It has great potential for improving applications currently based on a travel time approach such as in soil physics, hydrological and geotechnical engineering, by reducing the uncertainty associated with uncertain effective frequency in the single-valued apparent dielectric constant approach. The PVA-generated ADS can also provide a good starting dielectric model for more complete CDP inversion from full waveform. Further study in developing an algorithm considering multiple reflections is recommended to better tackle materials with high dielectric dispersion.

Acknowledgments

Funding for this research was partly provided by the Environmental Protection Administration, Taiwan.

References

[1] Sivagurunathan P, Dharmalingam K, Ramachandran K, Prabhakar Undre B, Khirade P W and Mehrotra S C 2007 Dielectric studies on binary mixtures of ester with alcohol using time domain reflectometry *J. Mol. Liq.* **133** 139–45
[2] Sun Z J, Young G D, McFarlane R A and Chambers B M 2000 The effect of soil electrical conductivity on moisture determination using time-domain reflectometry in sandy soil *Can. J. Soil Sci.* **80** 13–22
[3] Topp G C, Davis J L and Annan A P 1980 Electromagnetic determination of soil water content: measurements in coaxial transmission lines *Water Resour. Res.* **16** 574–82
[4] Previati M, Bevilacqua I, Canone D, Ferraris S and Haverkamp R 2010 Evaluation of soil water storage efficiency for rainfall harvesting on hillslope micro-basins built using time domain reflectometry measurements *Agric. Water Manage.* **97** 449–56
[5] Bois K J, Benally A D and Zoughi R 2000 Microwave near-field reflection property analysis of concrete for material content determination *IEEE Trans. Instrum. Meas.* **49** 49–55
[6] Hager N E and Domszy R C 2004 Monitoring of cement hydration by broadband time-domain-reflectometry dielectric spectroscopy *J. Appl. Phys.* **96** 5117
[7] Chung C-C and Lin C-P 2011 High concentration suspended sediment measurements using time domain reflectometry *J. Hydrol.* **401** 134–44
[8] Lin C-P, Tang S-H, Lin W-C and Chung C-C 2009 Quantification of cable deformation with time domain reflectometry—implications to landslide monitoring *J. Geotech. Geoenviron. Eng.* **135** 143–52
[9] Lin C, Lin C and Drnevich V 2012 TDR method for compaction quality control : multi evaluation and sources of error *Geotech. Test. J.* **35** 1–10
[10] Chung C-C, Lin C-S C, Wang K, Lin C-S C and Ngui Y J 2015 Improved TDR method for quality control of soil-nailing works *J. Geotech. Geoenviron. Eng.* **142** 1–4
[11] Santamarina J C, Klein K A and Fam M A 2001 *Soils and Waves* (New York: Wiley)
[12] Bottcher C J F and Bordewijk P 1978 *Theory of Electric Polarization* (Amsterdam: Elsevier)
[13] Giese K and Tiemann R 1975 Determination of the complex permittivity from thin-sample time domain reflectometry improved analysis of the step response waveform *Adv. Mol. Relax. Process.* **7** 45–59

[14] Clarkson T S, Glasser L, Tuxworth R W and Williams G 1977 An appreciation of experimental factors in time-domain spectroscopy *Adv. Mol. Relax. Interact. Process.* **10** 173–202
[15] Kaatze U 2013 Measuring the dielectric properties of materials. Ninety-year development from low-frequency techniques to broadband spectroscopy and high-frequency imaging *Meas. Sci. Technol.* **24** 012005
[16] Kaatze U 2008 Perspectives in dielectric measurement techniques for liquids *Meas. Sci. Technol.* **19** 112001
[17] Kaatze U 2010 Techniques for measuring the microwave dielectric properties of materials *Metrologia* **47** S91–113
[18] Cataldo A and De Benedetto E 2011 Broadband reflectometry for diagnostics and monitoring applications *IEEE Sens. J.* **11** 451–9
[19] Hager N E 1994 Broadband time-domain-reflectometry sampling dielectric spectroscopy using variable-time-scale sampling *Rev. Sci. Instrum.* **65** 887–91
[20] Roth K, Schulin R, Flühler H and Attinger W 1990 Calibration of time domain reflectometry for water content measurement using a composite dielectric approach *Water Resour. Res.* **26** 2267–73
[21] Dirksen C and Dasberg S 1993 Improved calibration of time domain reflectometry soil water content measurements *Soil Sci. Soc. Am. J.* **57** 660
[22] Lin C, Tang S and Chung C 2006 Development of TDR penetrometer through theoretical and laboratory investigations: 1. Measurement of soil dielectric permittivity *Geotech. Test. J.* **29** 306–13
[23] Hook W R and Livingston N J 1995 Propagation velocity errors in time domain reflectometry measurements of soil water *Soil Sci. Soc. Am. J.* **59** 92–6
[24] Chung C-C and Lin C-P 2009 Apparent dielectric constant and effective frequency of TDR measurements: influencing factors and comparison *Vadose Zo. J.* **8** 548
[25] Cataldo A, Tarricone L, Attivissimo F and Trotta A 2008 Simultaneous measurement of dielectric properties and levels of liquids using a TDR method *Measurement* **41** 307–19
[26] Lin C-P 2003 Frequency domain versus travel time analyses of TDR waveforms for soil moisture measurements *Soil Sci. Soc. Am. J.* **67** 720–9
[27] Dowding C, Summers J, Taflove A and Kath W 2002 Electromagnetic wave propagation model for differentiation of geotechnical disturbances along buried cables *Geotech. Test. J.* **25** 449–58
[28] Feng W, Lin C P, Deschamps R J and Drnevich V P 1999 Theoretical model of a multisection time domain reflectometry measurement system *Water Resour. Res.* **35** 2321
[29] Friel R and Or D 1999 Frequency analysis of time-domain reflectometry (TDR) with application to dielectric spectroscopy of soil constituents *Geophysics* **64** 707–18
[30] Heimovaara T J 1994 Frequency domain analysis of time domain reflectometry waveforms: 1. Measurement of the complex dielectric permittivity of soils *Water Resour. Res.* **30** 189–99
[31] Yanuka M, Topp G C, Zegelin S and Zebchuk W D 1988 Multiple reflection and attenuation of time domain reflectometry pulses: theoretical considerations for applications to soil and water *Water Resour. Res.* **24** 939–44
[32] Lin C P and Tang S H 2007 Comprehensive wave propagation model to improve TDR interpretations for geotechnical applications *Geotech. Test. J.* **30** 90–7
[33] Cataldo A, Catarinucci L, Tarricone L, Attivissimo F and Piuzzi E 2009 A combined TD–FD method for enhanced reflectometry measurements in liquid quality monitoring *IEEE Trans. Instrum. Meas.* **58** 3534–43
[34] Szypłowska A, Wilczek A, Kafarski M and Skierucha W 2016 Soil complex dielectric permittivity spectra determination using electrical signal reflections in probes of various lengths *Vadose Zo. J.* **15**
[35] Lin C-P, Tang S-H, Lin C-H and Chung C-C 2015 An improved modeling of TDR signal propagation for measuring complex dielectric permittivity *J. Earth Sci.* **26** 827–34
[36] Piuzzi E, Cataldo A, Cannazza G and De Benedetto E 2010 An improved reflectometric method for soil moisture measurement exploiting an innovative triple-short calibration *IEEE Trans. Instrum. Meas.* **59** 2747–54
[37] Ramo S, Whinnery J R and Van Duzer T 1994 *Fields and Waves in Communication Electronics* (New York: Wiley)
[38] Cole K S and Cole R H 1941 Dispersion and absorption in dielectrics I. Alternating current characteristics *J. Chem. Phys.* **9** 341
[39] Elmore W C and Heald M A 1985 *Physics of Waves* (New York: Dover)
[40] Skierucha W and Wilczek A 2010 A FDR sensor for measuring complex soil dielectric permittivity in the 10–500 MHz frequency range *Sensors* **10** 3314–29
[41] Hasted J B 1973 *Aqueous Dielectric* (New York: Chapman and Hall)